Calculation of Susceptibility Maps from Phase Image Data

A. Schäfer[1], S. Wharton[1], and R. Bowtell[1]

[1]Sir Peter Mansfield Magnetic Resonance Center, School of Physics and Astronomy, University of Nottingham, Nottingham, United Kingdom

Introduction

Recently it has been demonstrated that the phase of gradient echo images carries useful anatomical information which is linked to field perturbations due to the variation of susceptibility across different tissues (1,2). Generation of quantitative information from phase images is not straightforward, however, because of the non-local relationship between the field perturbation and susceptibility distribution (3). Here we show how this problem may be overcome via the calculation of a 3D map of the magnetic susceptibility variation from phase data. Such susceptibility maps could provide a useful new quantitative contrast in MRI yielding information for example about the variation of iron concentration across tissues. Unlike previously described approaches to the calculation of susceptibility variation from field maps (1,3,4) the method introduced here can be applied to complex objects, accommodates the effects of MR-invisible field sources and takes account of the effect of the sphere of Lorentz. The operation of the method has been demonstrated by application to simulated field maps from the brain and to experimental data acquired at 7 T from a simple phantom containing materials of different susceptibility.

Method

The magnetic field perturbation $\Delta B_z(\mathbf{r})$ generated by a susceptibility distribution $\chi(\mathbf{r})$ exposed to a z-directed magnetic field B_0 can be written in local form in the Fourier domain (Eqs.[1-4]) (3). This relation can be simply inverted to yield an expression describing the susceptibility in terms of the field perturbation (Eq. [5]). Inverse Fourier transformation of Eq. [5] then yields the susceptibility distribution (1,4). Although this is apparently a simple operation there are a number of potential pitfalls in using Eq. [5] to generate a susceptibility map.

{1} The denominator of Eq. [5] goes to zero when $\beta = 54.7^o$, so that there is a conical surface in k-space over which the susceptibility distribution, $\tilde{\chi}(\mathbf{k})$, cannot be evaluated. **{2}** In order to calculate $\Delta\tilde{B}_z(\mathbf{k})$ via Eq. [4] it is necessary to know the field perturbation, $\Delta B_z(\mathbf{r})$, over all space, whereas a phase map only provides information about the field perturbation in regions that generate an MR signal. **{3}** The field values that are measured in the MR-signal-generating regions include contributions from external sources which are not related to structures within the region of interest.

$$\Delta\tilde{B}_z(\mathbf{k}) = \frac{B_0\tilde{\chi}(\mathbf{k})}{3}\left(1-3\cos^2\beta\right) \quad [1]$$

$$\cos\beta = \frac{k_z}{|\mathbf{k}|} \quad [2]$$

$$\tilde{\chi}(\mathbf{k}) = \frac{1}{8\pi^3}\int d^3r\,\chi(\mathbf{r})\,e^{-i\mathbf{k}.V} \quad [3]$$

$$\Delta\tilde{B}_z(\mathbf{k}) = \frac{1}{8\pi^3}\int d^3r\,\Delta B_z(\mathbf{r})\,e^{-i\mathbf{k}.V} \quad [4]$$

$$\tilde{\chi}(\mathbf{k}) = \frac{3\Delta\tilde{B}_z(\mathbf{k})}{B_0\left(1-3\cos^2\beta\right)} \quad [5]$$

We have developed an iterative approach to reconstructing the susceptibility map in a defined region of interest (ROI) from measured phase/field data, which addresses the above problems in the following manner. **{1}** Measurement of a series of field maps with the object oriented at different angles with respect to the field allows a series of estimates of $\tilde{\chi}(\mathbf{k})$ to be formed via Eq. [5]. Rotation of the object with respect to the field changes the orientation of the conical surface over which the denominator of Eq. [5] goes to zero. Thus by averaging the estimates of $\tilde{\chi}(\mathbf{k})$ obtained for different field orientations, while excluding values in the regions where $\left(1-3\cos^2\beta\right)$ is close to zero, a faithful representation of $\tilde{\chi}(\mathbf{k})$ can be formed over all of k-space. **{2}** The field in external regions from which no MR signal is generated is estimated from a forward calculation of the field due to the current estimate of $\chi(\mathbf{r})$ in the ROI via Eq. [1] for each field orientation. **{3}** Since remote field sources generate slowly varying fields, subtraction of a low-order polynomial fit to the field maps measured in the ROI acts to attenuate the contributions of distant sources. To avoid eliminating the slowly varying fields that actually result from $\chi(\mathbf{r})$ in the ROI, a similar order polynomial fit to the field calculated in the ROI using the current estimate of $\chi(\mathbf{r})$ and Eq.[1] is added back into the measured data for each field orientation. Iterating this procedure yields an improving estimate of $\chi(\mathbf{r})$.

This approach was first tested by application to simulated field data calculated from a region spanning 60 axial slices in the brain of the 1mm resolution HUGO body model (Medical VR Studio, Lörrach). Tissue susceptibility values were taken from the literature [Grey Matter (GM): -8.97; White Matter (WM): -8.80; Bone: -8.4; CSF: -9.04; Fat: -7.79; Air: 0 all in ppm] (5). Field maps were calculated using Eq. [1] for angles of 0, 20, 40, 60 & 80° between B_o and the head-foot axis of the model. The method was also applied to phase maps measured from a phantom consisting of a 7 mm diameter tube, filled with an iron sulphate solution that was diluted so as to produce a susceptibility difference from water of 0.07 ppm (6), placed centrally in a 100 mm diameter water-filled sphere. The phantom was scanned on a 7T Philips Achieva scanner using a 3D spoiled gradient echo sequence with 1 mm isotropic resolution, 112 x 112 x 110 mm^3 FOV, TE/TR = 25/45 ms and $\alpha = 15^o$, in three different orientations (0, 13, 25° angles between tube axis and B_0). The phase maps acquired with different orientations were unwrapped and then aligned, based on parameters identified in co-registration of the modulus data.

Results and Discussion

The different steps of the calculation on data from the HUGO model are illustrated in Fig. 1. Figure 1A shows one slice from the model. Figures 1B-F show data from this slice for two different orientations of the model with respect to the field (0^o: upper panel; 60^o lower panel). Figure 1B = the calculated field perturbation; Fig. 1C = the 5th order polynomial fit to the field map in a central ROI; Fig. 1D = the result of subtracting the polynomial fit from the "measured" field, which reveals the local structure in the field perturbation; Fig. 1E = field map calculated from initial guess of $\chi(\mathbf{r})$ in the ROI (in this case a uniform susceptibility distribution); Fig. 1F= addition of Figs. 1D and 1E to produce a field map with appropriate field variation inside and outside the ROI; Fig. 1G = the final calculated susceptibility map.

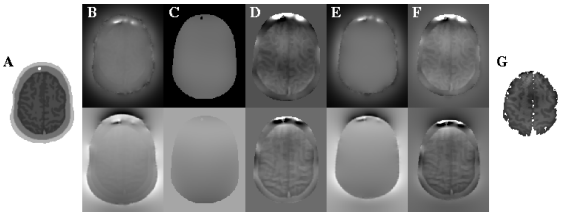

Figure 1: *Illustration of the different steps of the calculation for the HUGO model. See text for explanation.*

Figure 2, which shows the HUGO model and calculated susceptibility values from another slice, indicates more clearly that the calculated susceptibility map is a good representation of the original susceptibility distribution. Analysis of regions of interest yields a GM/WM susceptibility difference of -0.14 ± 0.08 ppm in good agreement with the literature value (5).

Figure 3 shows: (a) one slice of the modulus data from the phantom (the spherical masked region used in calculating the susceptibility map is shown in red); (b) the same slice in the calculated susceptibility map. ROI analysis on the susceptibility map yields a susceptibility difference between the tube and the sphere of 0.068 ± 0.009 ppm in good agreement with the expected difference.

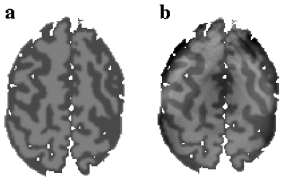

Figure 2: *Original HUGO susceptibility model (a) and calculated susceptibility map (b). For better visualization the maps are zoomed and masked to display only GM and WM .*

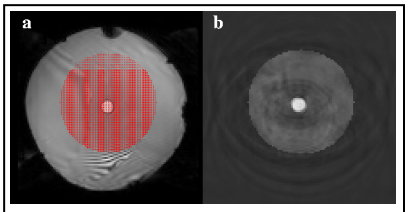

Figure 3: *Modulus image (a) and the susceptibility map (b) for the phantom. The spherical mask used for inversion is shown in (a) in red.*

References

[1] EM Haacke *et al* MRI 23: 1-25, 2005 **[2]** J Duyn *et al* PNAS 104:11796-11801, 2007 **[3]** JP Marques and R Bowtell, Conc. MR 25B: 65-78, 2005. **[4]** J Morgan. Proc ISMRM 15:35,2007 **[5]** CM Collins *et al* MRI 20:413-424, 2002 **[6]** DR Lide. CRC Handbook of Chemistry and Physics 2006/2007; Section 4:134-139.